

Light trajectories and wave dynamics in optical wormholes

Semra Gurtas Dogan^{1*}, Abdullah Guvendi^{2†}, Omar Mustafa^{3‡}

¹Department of Medical Imaging Techniques, Hakkari University, 30000, Hakkari, Türkiye

²Department of Basic Sciences, Erzurum Technical University, 25050, Erzurum, Türkiye

³Department of Physics, Eastern Mediterranean University, 99628, G. Magusa, north Cyprus, Mersin 10 - Türkiye

Abstract

We investigate the optical properties of a wormhole geometry characterized by a constant negative Gaussian curvature. This distinctive optical structure is modeled using the optical metric of the static BTZ black hole, corresponding to the hyperbolic wormhole framework. Within this model, we derive the arbitrary geodesics and the associated effective potential. Our analysis reveals that the effective potential becomes increasingly narrow as the curvature radius of the optical wormhole decreases, with all possible trajectories converging at the optical origin $\rho = 0$. We further analyze the wave modes governing light propagation on this curved surface, demonstrating that the effective potential is purely repulsive in both the small and large ρ limits. While the potential remains finite in both regimes, its behavior differs markedly. Near the optical origin, the magnetic quantum number (m) exerts a significant influence on the effective repulsive potential, particularly for large values of m , where the potential resembles a typical barrier. However, this effect diminishes with increasing optical distance. Using this framework, we compute the reflection and transmission coefficients for $m \neq 0$. Our findings indicate that the optical properties of the background are predominantly governed by the curvature radius of the optical wormhole, highlighting its critical role in shaping light propagation in such geometries.

Keywords: Optical wormholes; BTZ black holes; Light propagation; Effective potential; Ray geodesics; Curvature effects

Introduction

The BTZ black hole, introduced by Bañados, Teitelboim, and Zanelli, offers an exact solution to Einstein's field equations in (2+1)-dimensional spacetime with a negative cosmological constant, $\Lambda = -\frac{1}{l^2}$, where l represents the radius of AdS_3 spacetime [1]. Characterized by its mass parameter M and the cosmological constant, the static BTZ black hole lacks angular momentum and electric charge, resulting in a spacetime with a static, asymptotically anti-de Sitter (AdS) geometry and a well-defined horizon structure [2]. The metric of this black hole, in standard coordinates (t, r, ϕ) , is expressed as [1, 2]:

$$ds^2 = -\left(-M + \frac{r^2}{l^2}\right) dt^2 + \left(-M + \frac{r^2}{l^2}\right)^{-1} dr^2 + r^2 d\phi^2,$$

where t , r , and ϕ denote the time, radial, and angular coordinates, respectively. The term $-M + \frac{r^2}{l^2}$ determines the spacetime's causal structure, with the event horizon located at $r_+ = l\sqrt{M}$ for $M > 0$. Due to the absence of angular momentum, the static BTZ spacetime is devoid of inner horizons or ergoregions, offering a simpler geometry compared to its rotating counterpart. This simplicity, coupled with the preservation of key features such as the event horizon, thermodynamic properties, and causal structure, makes the static BTZ black hole a compelling model for studying lower-dimensional gravity [2]. Its mathematical tractability has enabled extensive investigations into black hole thermodynamics [2, 3], quantum gravity [3], holographic superconductivity [4], and quantum criticality within the $\text{AdS}_3/\text{CFT}_2$ correspondence framework [5].

Interestingly, the BTZ black hole has found relevance in condensed matter physics, particularly in graphene systems [6]. By mapping its conformal counterpart

onto the Beltrami pseudosphere, researchers have drawn analogies between (2+1)-dimensional gravity and the curved geometry of monolayer graphene [6–8]. For instance, the optical metric of the static BTZ black hole corresponds to a curved surface with constant negative Gaussian curvature, mirroring the geometry of monolayer graphene sheets. Recent studies have revealed that this (2+1)-dimensional spacetime represents an optical wormhole, or hyperbolic wormhole, characterized by constant negative Gaussian curvature [9–11]. These studies demonstrate that the tunneling time of charge carriers and photons can be manipulated by varying the curvature radius along the radial coordinate of the optical wormhole [9–11]. Consequently, determining the effective repulsive background potentials governing ray and wave propagation is of significant interest for developing advanced photonic and nanoscale devices. The versatility of graphene-based systems, which can be curved, twisted, or rolled to meet specific design requirements, further underscores their potential in applications such as ultrafast photodetectors [12].

On the other hand, exploring geodesics and wave dynamics in curved spaces provides a powerful framework for analyzing optical effects induced by effective background potentials [13, 14]. In general relativity, massive objects warp spacetime, altering electromagnetic wave propagation. This curvature-driven wave dynamics has implications for wave optics [15], gravitational lensing [16], scattering theory [17], and photon ring studies [18, 19]. However, optical investigations of these phenomena remain limited due to the weak nature of gravitational effects, necessitating astronomical-scale observations. To overcome these challenges, analog models have been proposed to simulate general relativistic effects in laboratory settings [21]. Examples include observing spontaneous Hawking radiation in Bose–Einstein condensates [22], simulating Schwarzschild precession with gradient-index lenses [23], and replicating gravitational lensing using microstructured optical waveguides [24]. An alternative approach involves reducing the spatial dimensions of curved spacetimes while embedding them in flat three-dimensional space, enabling detailed studies of electromagnetic wave interactions with curvature [25, 26]. This approach, pioneered by Batz and Peschel [27], has inspired theoretical and experimental investigations across diverse optical phenomena [12, 20, 28, 29]. Applications have extended to surface plasmon polaritons [30] and quantum particles [31]. Initially, Batz and Peschel derived a nonlinear Schrödinger equation for light propagation on surfaces of revolution with constant Gaussian curvature [27]. While rotational symmetry simplifies curvilinear coordinate descriptions [32], their solution is restricted to longitudinal propagation, leaving non-longitudinal trajectories analytically challenging. Nevertheless, longitudinal propagation benefits from axisymmetric curvature, ensuring tangential light beams follow the longitudinal path [20].

In this study, we analyze the geodesics and wave dynamics within an optical wormhole described by the static BTZ black hole's optical metric. This metric represents a hyperbolic wormhole with constant negative curvature. Section 2 revisits the underlying ultra-static spacetime structure. Section 3 examines light trajectories, while Section 4 extends the analysis to wave dynamics by solving the Helmholtz equation. We highlight the role of effective background potentials, noting their finite repulsive nature near the optical origin. For specific scenarios, these potentials are modeled as simple barrier potentials, enabling the derivation of reflection and transmission coefficients in Section 4.1. Finally, Section 5 summarizes the findings and discusses their broader implications.

2 Revisiting the BTZ optical metric

Recent studies [6, 7] propose that a graphene structure shaped as a surface of revolution with constant negative curvature, such as the Beltrami trumpet, may ex-

* E-mail: semragurtasdogan@hakkari.edu.tr (Corr. Author)

† E-mail: abdullah.guvendi@erzurum.edu.tr

‡ E-mail: omar.mustafa@emu.edu.tr

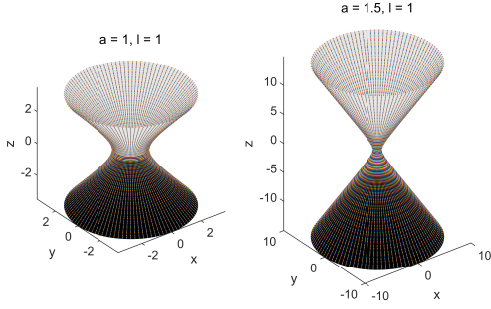


Figure 1: Visualization of the wormhole geometry for varying parameter values. The coordinates are defined by $x(\rho, \phi) = l \sinh\left(\frac{a}{l}\rho\right) \cos(\phi)$, $y(\rho, \phi) = l \sinh\left(\frac{a}{l}\rho\right) \sin(\phi)$, and $z(\rho) = \pm \int d\rho \sqrt{1 - (\eta'(\rho))^2}$, where the prime denotes the derivative with respect to ρ .

hibit phenomena analogous to those observed in quantum field theory on curved spacetimes. Of particular interest is the potential connection to BTZ black hole metrics [1]. These solutions have been extensively studied due to their significance in string theory, particularly in the context of black holes and their quantum microstates. The metric of the static BTZ black hole can be rewritten as follows:

$$ds_{\text{BTZ}}^2 = -\Delta dt^2 + \frac{dr^2}{\Delta} + r^2 d\phi^2, \quad (2.1)$$

where

$$\Delta(r) = \frac{r^2}{l^2} - M. \quad (2.2)$$

It is well established (refer to [33] for a comprehensive review) that low-energy electronic excitations on a curved graphene sheet Σ obey the massless Dirac equation on $\mathbb{R} \times \Sigma$ with respect to the induced metric:

$$ds^2 = -dt^2 + h_{ij} dx^i dx^j, \quad i = 1, 2, \quad (2.3)$$

where, h_{ij} denotes the metric induced on the surface Σ . The scenario examined in [6] involves a surface of revolution embedded in the Euclidean three-space \mathbb{E}^3 , with coordinates $(x(x^i), y(x^i), z(x^i))$. The metric given in (2.3) represents an ultra-static metric, characterized as both static and invariant under time translations and time reversal. The general form of a static metric is:

$$ds^2 = -V dt^2 + g_{ij} dx^i dx^j. \quad (2.4)$$

For static black holes, we have $V > 0$ outside the horizon. A metric is termed ultra-static if $V = 1$, implying the absence of gravitational redshift and that gravitational forces do not act on a particle at rest in such a spacetime. Since graphene does not exhibit an apparent source of redshifting, the assumption in [6] that $g_{tt} = -1$ is physically well-founded. It is important to emphasize that a black hole metric cannot be ultra-static. However, the massless Dirac equation remains invariant under conformal rescalings [7]. Specifically, in D spacetime dimensions, if

$$\tilde{g}_{\mu\nu} = \Omega^2 g_{\mu\nu}, \quad \tilde{\Psi} = \frac{1}{\Omega^{(D-1)/2}} \Psi, \quad (2.5)$$

then the equation transforms into:

$$\gamma^\mu \nabla_\mu \Psi = \frac{1}{\Omega^{(D+1)/2}} \tilde{\gamma}^\mu \tilde{\nabla}_\mu \Psi. \quad (2.6)$$

Furthermore, any static metric is locally conformally ultra-static:

$$-V dt^2 + g_{ij} dx^i dx^j = V \{-dt^2 + h_{ij} dx^i dx^j\}, \quad (2.7)$$

where $h_{ij} = \frac{1}{V} g_{ij}$ is referred to as the optical metric [34]. This observation implies that, at least in classical contexts, the effects of horizons on massless fermions can be simulated using ultra-static metrics for graphene, as proposed in [6]. However, in quantum field theory, the vacuum state is not necessarily invariant under conformal transformations, making the simulation of Unruh or Hawking radiation

effects non-trivial. It is also important to note that not all time-independent (stationary) metrics are static. For example, static black holes in $2 + 1$ dimensions, including static BTZ black holes, are stationary. Their metrics generally take the form:

$$ds^2 = -V dt^2 + g_{ij} dx^i dx^j. \quad (2.8)$$

Locally, any stationary metric can be transformed into one of two forms via conformal rescaling [34]. The first form is expressed as:

$$ds_R^2 = -dt^2 + a_{ij} dx^i dx^j, \quad (2.9)$$

where $a_{ij} = V^{-1} g_{ij}$. Alternatively, by applying a different conformal rescaling and completing the square, the corresponding form is:

$$ds^2 = -dt^2 + h_{ij} dx^i dx^j, \quad (2.10)$$

where h_{ij} represents the optical metric [34]. The static BTZ black hole metric, given in (2.1), is already in the optical form, apart from a conformal factor Δ [7]. From this point, we focus on axisymmetric metrics that can be isometrically embedded into Euclidean space \mathbb{E}^3 as surfaces of revolution. These metrics are described by [7]:

$$h_{ij} dx^i dx^j = d\rho^2 + C^2(\rho) d\phi^2, \quad 0 \leq \phi < 2\pi, \quad (2.11)$$

where $C^2(\rho) = x^2 + y^2 = R^2$ and $d\rho^2 = dR^2 + dz^2$. The Gaussian curvature (K) [35] is given by:

$$K = -\frac{\ddot{C}(\rho)}{C(\rho)}, \quad (2.12)$$

where the dot denotes differentiation with respect to the variable ρ . The Beltrami trumpet, as introduced in [6], serves as an example of such a surface [7]:

$$C(\rho) = a \exp\left(-\frac{\rho}{a}\right), \quad \rho \geq 0 \implies K = -\frac{1}{a^2}. \quad (2.13)$$

For the static BTZ metric given by equation (2.1), where $0 \leq \phi < 2\pi$, the corresponding optical metric is expressed as

$$ds_o^2 = -dt^2 + \frac{dr^2}{\Omega^2} + \frac{r^2}{\Omega^2} d\phi^2, \quad \Omega^2 = \frac{r^2}{l^2} - M. \quad (2.14)$$

We now proceed to embed the exact static BTZ optical geometry into E^3 , beginning with the static BTZ optical geometry in equation (2.14). The metric is then expressed as follows:

$$ds_o^2 = -dt^2 + \frac{l^4}{(r^2 - a^2)^2} dr^2 + \frac{l^2}{r^2(r^2 - a^2)} d\phi^2, \quad (2.15)$$

where $a = l\sqrt{M}$. Defining $C^2 = \frac{l^2 r^2}{r^2 - a^2}$, we can rewrite the following relations (for more details see [7]):

$$\begin{aligned} dz^2 + dC^2 &= \frac{l^4}{(r^2 - a^2)^2} dr^2 \\ \Rightarrow dz^2 &= l^2 \frac{(r^2 - a^2(l^2 + a^2))}{(r^2 - a^2)^3} dr^2. \end{aligned} \quad (2.16)$$

This yields

$$\left(\frac{dz}{dC}\right)^2 = \frac{1 + \frac{l^2}{a^2} - \frac{C^2}{l^2}}{C^2 - l^2}. \quad (2.17)$$

Equation (2.17) implies that the embedding process must terminate when $C = \sqrt{l^2 + a^2}$, which corresponds to a radius beyond the horizon where $C^2 \rightarrow \infty$. The radial optical distance, ρ , is then defined by $d\rho = \frac{l^2 r^2}{r^2 - a^2} dr$, and implies the following relationships: $r = a \coth\left(\frac{a}{l}\rho\right)$, and $C = l \cosh\left(\frac{a}{l}\rho\right)$ [7]. Thus, the optical metric takes the form [7, 9–11]:

$$ds_o^2 = -dt^2 + d\rho^2 + l^2 \cosh^2\left(\frac{a}{l}\rho\right) d\phi^2, \quad (2.18)$$

while the BTZ metric itself is given by [7]:

$$\begin{aligned} ds_{\text{BTZ}}^2 &= \mathcal{Q}(\rho) \left[-dt^2 + d\rho^2 + l^2 \cosh^2\left(\frac{a}{l}\rho\right) d\phi^2\right], \\ \mathcal{Q}(\rho) &= a^2 \sinh^2\left(\frac{a}{l}\rho\right). \end{aligned} \quad (2.19)$$

It is worth noting that the Gaussian curvature of the spatial part of the BTZ optical metric is constant and negative [9–11]. By interpreting l as the radius of the wormhole at the midpoint ($\rho = 0$) between two sheets, and l/a as the radius of curvature along $\hat{\rho}$ of the graphene wormhole connecting the two monolayer sheets, the metric in equation (2.18) characterizes a hyperbolic wormhole with constant negative Gaussian curvature [9–11]. The geometric structure of this wormhole can be seen in Figure 1.

3 Ray optics

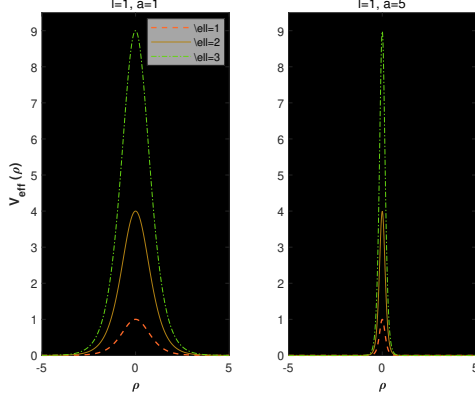


Figure 2: Plot of the effective potential as a function of the radial coordinate ρ over the range $\rho \in [-5, 5]$, calculated using Eq. (3.7) for $\ell = 1$, $\ell = 2$, and $\ell = 3$.

In this section, we examine the light propagation in the geometric background described by the metric given in (2.18). We begin by studying the geodesic equation to determine the light ray trajectories. To find the geodesics, we follow the approach outlined in Refs. [13, 14], where both null and timelike geodesics are determined. We take the Lagrangian as

$$\mathcal{L} = g_{\mu\nu} \frac{dx^\mu}{d\lambda} \frac{dx^\nu}{d\lambda}, \quad g_{\mu\nu} = \text{diag}(-1, 1, \eta(\rho)^2), \quad (\mu, \nu = t, \rho, \phi), \quad \eta(\rho) = l \cosh\left(\frac{a}{l}\rho\right), \quad (3.1)$$

where λ is the affine parameter of the curve, and the geodesics are obtained as solutions of the Euler-Lagrange equation:

$$\frac{\partial \mathcal{L}}{\partial x^\mu} - \frac{d}{d\lambda} \left(\frac{\partial \mathcal{L}}{\partial \dot{x}^\mu} \right) = 0. \quad (3.2)$$

Now, set $\mathcal{L} = \tilde{\kappa}$ by taking the speed of light (c) in vacuum as unity, $c = 1$. It should be noted that the choice $\tilde{\kappa} = 0$ corresponds to lightlike geodesics, while $\tilde{\kappa} = -1$ yields timelike geodesics. Using the line element in Eq. (2.18), the Lagrangian becomes

$$\mathcal{L} = -\dot{t}^2 + \dot{\rho}^2 + \eta^2 \dot{\phi}^2, \quad (3.3)$$

where the dot indicates a derivative with respect to the affine parameter λ . Since \mathcal{L} does not explicitly depend on t and ϕ , the derivatives $\frac{\partial \mathcal{L}}{\partial t}$ and $\frac{\partial \mathcal{L}}{\partial \phi}$ are constants of motion, corresponding to the following conserved quantities, respectively:

$$\mathcal{E} = \dot{t}, \quad \ell = \eta^2 \dot{\phi}. \quad (3.4)$$

In terms of \mathcal{E} and ℓ , we can rewrite the Lagrangian as follows:

$$\mathcal{L} = -\mathcal{E}^2 + \dot{\rho}^2 + \frac{\ell^2}{\eta(\rho)^2}. \quad (3.5)$$

For null geodesics ($\tilde{\kappa} = 0$), we obtain

$$\left(\frac{d\rho}{d\lambda} \right)^2 = \mathcal{E}^2 - \frac{\ell^2}{\eta(\rho)^2}. \quad (3.6)$$

This equation can be interpreted as one-dimensional motion of a particle (with energy \mathcal{E}) under the influence of an effective potential given by (see also [14])

$$V_{\text{eff}}(\rho) = \frac{\ell^2}{l^2 \cosh^2\left(\frac{a}{l}\rho\right)}. \quad (3.7)$$

This effective potential is a classic example of a Pöschl-Teller potential, widely studied for its exact solvability and relevance in quantum systems. This potential exhibits a finite, localized peak centered at $\rho = 0$, where it attains its maximum value of $V_{\text{eff}}(0) = \frac{\ell^2}{l^2}$. The $\cosh^2\left(\frac{a}{l}\rho\right)$ term governs the spatial decay, ensuring that the potential decreases symmetrically and rapidly toward zero as $|\rho| \rightarrow \infty$. This asymptotic behavior reflects the diminishing influence of the potential at large distances, making it effective only within a finite region around the origin. The

parameter ℓ determines the strength of the peak, while l and a influence its width and the decay rate. Physically, this potential describes a repulsive interaction that prevents particles from occupying the central region, with no attractive well or bound-state solutions. Its resemblance to the hyperbolic secant-squared function underscores its utility in modeling systems with localized barriers, such as scattering processes or field-theoretic solitonic structures. Additionally, our results imply that radial motion occurs only when $\frac{d\rho}{d\lambda} > 0$, as the condition $\mathcal{E}^2 < \frac{\ell^2}{\eta(\rho)^2}$ is prohibited for radial motion. The behavior of the effective potential $V_{\text{eff}}(\rho)$ is illustrated in Figure 2 for $\ell = 1$, $\ell = 2$, and $\ell = 3$. As depicted, these values of ℓ do not exhibit any stable equilibrium points. Furthermore, the figure indicates a significant reduction in the tunneling time of charge carriers as the radius of curvature (ℓ/a) of the optical wormhole connecting two monolayer sheets decreases. This observation aligns with the findings reported in Ref. [9] for Weyl pairs in an optical wormhole background. For further details, refer to [9] and [10]. A similar effect has also been observed for photons (massless vector bosons) in such static optical wormholes, as discussed in [11].

Now, for arbitrary geodesics, we can obtain the following expression:

$$\dot{\phi} = \frac{1}{\eta(\rho) \sqrt{\frac{(\tilde{\kappa} + \mathcal{E}^2)}{\ell^2} \eta(\rho)^2 - 1}} \dot{\rho}. \quad (3.8)$$

This leads to the following result:

$$\phi(\rho) = \phi(\rho_i) \pm \int_{\rho_i}^{\rho} \frac{d\rho}{\eta(\rho) \sqrt{\frac{(\tilde{\kappa} + \mathcal{E}^2)}{\ell^2} \eta(\rho)^2 - 1}}. \quad (3.9)$$

The solution for $\phi(\rho)$ is obtained as follows:

$$\begin{aligned} \phi(\rho) &= \tilde{\phi}(\rho_i) \pm \frac{\ln \epsilon(\rho)}{a}, \\ \epsilon(\rho) &= \frac{\tanh\left(\frac{a}{l}\rho\right)}{\sqrt{\tilde{a}}} + \sqrt{1 + \frac{\tanh^2\left(\frac{a}{l}\rho\right)}{\tilde{a}}}, \\ \tilde{a} &= \frac{l^2}{\ell^2} (\tilde{\kappa} + \mathcal{E}^2) - 1, \end{aligned} \quad (3.10)$$

and the trajectories are illustrated in Figures 3-4.

4 Wave optics

In the previous section, we derived the trajectories of light in the effective geometry of the optical wormhole. Now, we examine the corresponding propagating wave modes. Let us start by writing the Helmholtz equation in an effective geometry [14]:

$$(\nabla_g + k^2)\Psi = 0, \quad (4.1)$$

where ∇_g is the Laplace-Beltrami operator and k is the wave number. For a generic metric $ds^2 = g_{ij}dx^i dx^j$, the Laplace-Beltrami operator is given by

$$\nabla_g \Psi = \frac{1}{\sqrt{g}} \partial_i (\sqrt{g} g^{ij} \partial_j \Psi), \quad (4.2)$$

where $g = |\det(g_{ij})|$, $i, j = \rho, \phi$. According to Eq. (2.18), the corresponding Helmholtz equation is obtained as follows:

$$\left[\partial_\rho^2 + \frac{a}{l} \tanh\left(\frac{a}{l}\rho\right) \partial_\rho + k^2 - \frac{m^2}{l^2 \cosh^2\left(\frac{a}{l}\rho\right)} \right] \psi(\rho) = 0, \quad (4.3)$$

if $\Psi(\rho, \phi) = \psi(\rho) e^{im\phi}$, where $m = 0, \pm 1, \pm 2, \dots$ due to the periodic boundary condition on ϕ . Let us now determine the effective potential for waves propagating in the optical wormhole background. To achieve this, we eliminate the first-order derivative term by defining:

$$\psi(\rho) = e^{-\frac{1}{2} \int \frac{a}{l} \tanh\left(\frac{a}{l}\rho\right) d\rho} \varphi(\rho). \quad (4.4)$$

The exponential factor is carefully selected to ensure that, upon differentiation of $\psi(\rho)$, the first-order derivative term cancels out seamlessly. This leads to the following simplified equation:

$$\ddot{\varphi}(\rho) + [k^2 - V_{\text{eff}}(\rho)] \varphi(\rho) = 0, \quad (4.5)$$

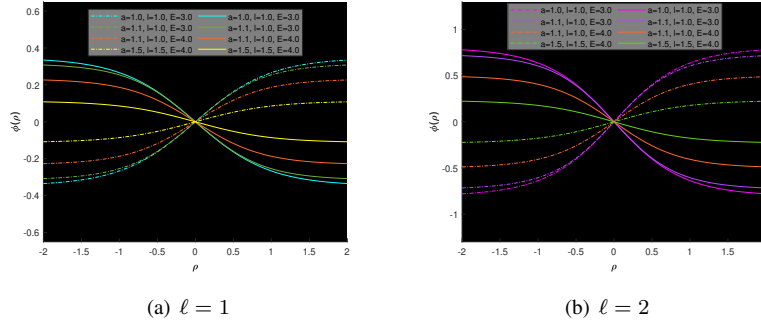


Figure 3: Trajectories are plotted over the range $-2 \leq \rho \leq 2$, showcasing variations in the parameters a , for l and \mathcal{E} . The calculations are carried out with fixed parameter $\tilde{\kappa} = 0$, and an initial condition $\phi(\rho_i) = 0$

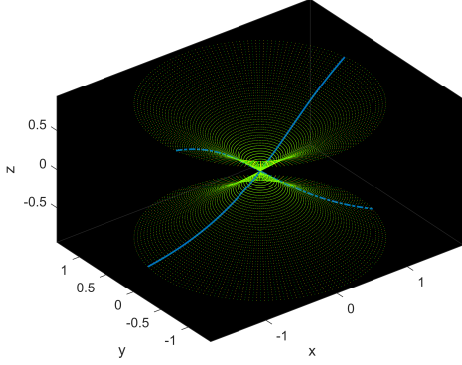


Figure 4: Plots of ray geodesics on the optical wormhole surface for $a = 1.2$ and $l = 1.2$ for varying ρ in the range of $[-1, 1]$. Here, we take $\mathcal{E} = 3$, $\ell = 1$ and $\tilde{\kappa} = 0$.

where

$$V_{\text{eff}}(\rho) = \frac{a^2}{4l^2} + \frac{\frac{a^2}{4} + m^2}{l^2 \cosh^2\left(\frac{a}{l}\rho\right)}. \quad (4.6)$$

Eq. (4.5) is a Schrödinger-like equation for the unknown function $\varphi(\rho)$, with the effective potential given by Eq. (4.6). The profile of this effective potential is shown in Figure 5, which exhibits a trend similar to that in Figure 2. The effective potential (4.6) exhibits a repulsive nature, characterized by its peaked structure around $\rho = 0$ and a rapid decay toward a finite constant at asymptotically large $|\rho|$. The term $\frac{a^2}{4l^2}$ introduces a uniform energy shift, raising the baseline of the potential, while the second term, proportional to $\cosh^{-2}\left(\frac{a}{l}\rho\right)$, dominates the spatial dependence. At $\rho = 0$, where $\cosh^2\left(\frac{a}{l}\rho\right) = 1$, the potential reaches its maximum value of

$$V_{\text{eff}}(0) = \frac{a^2/2 + m^2}{l^2} = V_0 > 0 \quad (\text{constant}). \quad (4.7)$$

In this limit, we can consider the width of the constant potential barrier to be $2l$, where l represents the radius of the wormhole at the midpoint ($\rho = 0$). In this case, the solutions to Eq. (4.5) are given by

$$\varphi(\rho) = C_1 \sin(\tilde{k}\rho) + C_2 \cos(\tilde{k}\rho), \quad (4.8)$$

where $\tilde{k} = \sqrt{k^2 - V_0}$. This indicates that the solution functions exhibit oscillatory behavior when $k^2 > V_0$, and in this case, we can re-express the solutions in the following form:

$$\varphi(\rho) = A e^{i\tilde{k}\rho} + B e^{-i\tilde{k}\rho}. \quad (4.9)$$

However, if $k^2 < V_0$, the solution functions become

$$\varphi(\rho) = C e^{\kappa\rho} + D e^{-\kappa\rho}. \quad (4.10)$$

If $|\rho|$ is large, the $\cosh^2\left(\frac{a}{l}\rho\right)$ terms in the effective potential grow significantly, causing the terms $\propto \cosh^{-2}\left(\frac{a}{l}\rho\right)$ to rapidly decay to zero. Consequently, the potential approaches the constant value

$$\lim_{|\rho| \rightarrow \infty} V_{\text{eff}} = \frac{a^2}{4l^2} > 0. \quad (4.11)$$

In this case, the effective potential is independent of the magnetic quantum number m , and the corresponding physical solution can be written as

$$\varphi(\rho) = \mathcal{F} e^{ik_1\rho}, \quad (4.12)$$

where $k_1 = \sqrt{k^2 - \frac{a^2}{4l^2}}$. This means that the solution functions also exhibit oscillatory behavior when $k^2 > \frac{a^2}{4l^2}$, or solutions decay exponentially if $k < \frac{a}{2l}$. This behavior also indicates that the potential is purely repulsive, with no attractive region or potential well that could trap particles. The barrier at $\rho = 0$ represents the strongest repulsion (especially for large m), discouraging the localization at the center. At large distances, the potential becomes effectively constant, implying that the repulsion diminishes but remains non-zero. Such a potential is consistent with systems where a central repulsive force dominates, preventing bound states and promoting scattering dynamics. The mathematical form of the effective potential in Eq. (4.6), reminiscent of the repulsive Pöschl-Teller potential, highlights its utility in modeling repulsive interactions in theoretical frameworks with finite asymptotic energy contributions.

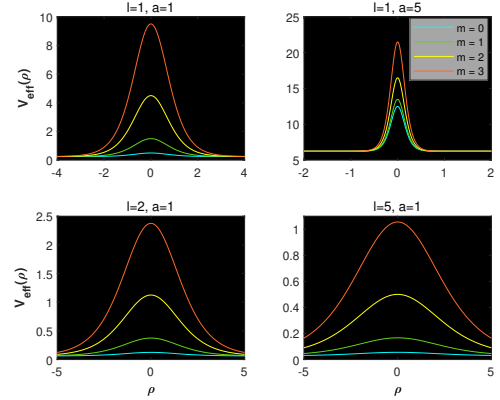


Figure 5: Effective potential $V_{\text{eff}}(\rho)$ plotted as a function of ρ for different parameter combinations of a and l , with $m = 0, 1, 2, 3$. For all cases, the potential lacks minima for the chosen m values but displays a pronounced maximum at $\rho = 0$. Asymptotically, $V_{\text{eff}}(\rho)$ approaches zero, with the height of the central barrier increasing as m grows larger. Additionally, narrower potential barriers are observed for smaller curvature radius (l/a).

4.1 A specific scenario

Consider the effective potential as a barrier potential within the region $\rho \in [0, L]$, where the width is $L = 2l$ and the magnitude is V_0 , satisfying the condition $V_0 > k^2$, particularly for large values of m . Under these conditions, the system reduces to a one-dimensional barrier potential problem in quantum mechanics. In this framework, the wave number may be represented by k_1 for waves outside the barrier region, arising from the non-vanishing continuous effective potential $V_{\text{eff}} = \frac{a^2}{4l^2} > 0$. Assuming the case $k_1 > 0$, the wave function can be expressed

as follows

$$\begin{aligned}\varphi(\rho) &= \mathcal{A}e^{ik_1\rho} + \mathcal{B}e^{-ik_1\rho} \quad \text{for } \rho < 0, \\ \varphi(\rho) &= \mathcal{C}e^{\kappa\rho} + \mathcal{D}e^{-\kappa\rho} \quad \text{for } 0 < \rho < L, \\ \varphi(\rho) &= \mathcal{F}e^{ik_1\rho} \quad \text{for } \rho > L.\end{aligned}\quad (4.13)$$

The continuity conditions at $\rho = 0$ yield:

$$\begin{aligned}\mathcal{A} &= \frac{\kappa + ik_1}{2ik_1}\mathcal{C} + \frac{-\kappa + ik_1}{2ik_1}\mathcal{D}, \\ \mathcal{B} &= \frac{-\kappa + ik_1}{2ik_1}\mathcal{C} + \frac{\kappa + ik_1}{2ik_1}\mathcal{D},\end{aligned}\quad (4.14)$$

and at $\rho = L$ give:

$$\begin{aligned}\mathcal{C} &= \frac{\kappa + ik_1}{2\kappa}\mathcal{F}e^{ik_1L}e^{-\kappa L}, \\ \mathcal{D} &= \frac{\kappa - ik_1}{2\kappa}\mathcal{F}e^{ik_1L}e^{\kappa L}.\end{aligned}\quad (4.15)$$

By substituting the results from Eq. (4.15) into Eq. (4.14), we obtain:

$$\begin{aligned}\mathcal{A} &= \frac{e^{ik_1L}}{4ik_1\kappa} (4ik_1\kappa \cosh(\kappa L) + 2(k_1^2 - \kappa^2) \sinh(\kappa L)) \mathcal{F}, \\ \mathcal{B} &= \frac{e^{ik_1L}}{4ik_1\kappa} (2(k_1^2 + \kappa^2) \sinh(\kappa L)) \mathcal{F}.\end{aligned}\quad (4.16)$$

From these results, we can compute the ratios $\frac{\mathcal{F}}{\mathcal{A}}$ (the amplitude ratio of the transmitted wave to the incident wave) and $\frac{\mathcal{B}}{\mathcal{A}}$ (the amplitude ratio of the reflected wave to the incident wave). The expressions for these ratios are:

$$\begin{aligned}\frac{\mathcal{F}}{\mathcal{A}} &= \frac{4ik_1\kappa}{e^{ik_1L} (4ik_1\kappa \cosh(\kappa L) + 2(k_1^2 - \kappa^2) \sinh(\kappa L))}, \\ \frac{\mathcal{B}}{\mathcal{A}} &= \frac{2(k_1^2 + \kappa^2) \sinh(\kappa L)}{4ik_1\kappa \cosh(\kappa L) + 2(k_1^2 - \kappa^2) \sinh(\kappa L)}.\end{aligned}\quad (4.17)$$

Hence, the transmission coefficient $T = \left| \frac{\mathcal{F}}{\mathcal{A}} \right|^2$ is calculated as:

$$T = \frac{4k_1^2\kappa^2}{(4k_1^2\kappa^2 \cosh^2(\kappa L) + (k_1^2 - \kappa^2)^2 \sinh^2(\kappa L))}. \quad (4.18)$$

This result implies that the transmission coefficient decreases exponentially as L increases, which corresponds to an increase in the radius of the optical wormhole. Additionally, we can calculate the reflection coefficient $R = \left| \frac{\mathcal{B}}{\mathcal{A}} \right|^2$ as:

$$R = \frac{(k_1^2 + \kappa^2)^2 \sinh^2(\kappa L)}{(4k_1^2\kappa^2 \cosh^2(\kappa L) + (k_1^2 - \kappa^2)^2 \sinh^2(\kappa L))}. \quad (4.19)$$

The values of these coefficients are shown in Figure 6. Moreover, one can easily verify that the relation $R + T = 1$ holds. The numerator reads:

$$\begin{aligned}& 4k_1^2\kappa^2 + (k_1^2 + \kappa^2)^2 \sinh^2(\kappa L) \\ &= 2k_1^2\kappa^2 \cosh^2(\kappa L) + 2k_1^2\kappa^2 + (k_1^4 + \kappa^4) \sinh^2(\kappa L) \\ &\quad + 2k_1^2\kappa^2 \sinh^2(\kappa L) - 2k_1^2\kappa^2 \sinh^2(\kappa L) \\ &= 4k_1^2\kappa^2 \cosh^2(\kappa L) + (k_1^2 - \kappa^2)^2 \sinh^2(\kappa L),\end{aligned}\quad (4.20)$$

which is identical to the denominator, thus confirming that $R + T = 1$.

For a fixed value of a , increasing L corresponds to a larger l , which in turn leads to a larger radius of curvature for the optical wormhole. This suggests that the tunneling time for particles through these effective potentials becomes longer (or shorter) as the radius of curvature increases (or decreases). This conclusion is consistent with the findings in Refs. [9–11].

5 Summary and discussions

In this paper, we investigate the ray trajectories and wave dynamics in the optical static BTZ metric. This spacetime is in ultra-static form and corresponds to a hyperbolic wormhole, also referred to as an optical wormhole, described by negative constant Gaussian curvature. Such curved spacetimes provide an excellent framework for studying phenomena such as Hawking-Unruh effects, charge carrier

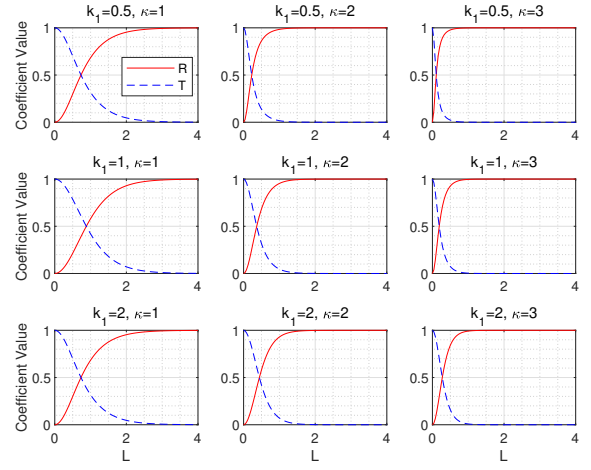


Figure 6: Reflection (R) and transmission (T) coefficients as functions of the length L for various values of k_1 and κ . The coefficients are plotted for $k_1 = 0.5, 1, 2$ and $\kappa = 1, 2, 3$, illustrating how the reflection and transmission behavior changes with these parameters.

evolution, and decaying photonic modes in monolayer graphene sheets and optical wormholes (see Figure 1).

We begin by examining ray optics and wave optics in this curved space. The trajectories are obtained analytically as follows:

$$\begin{aligned}\phi(\rho) &= \tilde{\phi}(\rho_i) \pm \frac{\ln \epsilon(\rho)}{a}, \\ \epsilon(\rho) &= \frac{\tanh\left(\frac{a}{\ell}\rho\right)}{\sqrt{\frac{l^2}{\ell^2}(\kappa + \mathcal{E}^2) - 1}} + \sqrt{1 + \frac{\tanh^2\left(\frac{a}{\ell}\rho\right)}{\frac{l^2}{\ell^2}(\kappa + \mathcal{E}^2) - 1}},\end{aligned}\quad (5.1)$$

with the corresponding ray trajectories ($\kappa \approx 0$) depicted in Figures 3, and 4. The behavior of $\epsilon(\rho)$ is as follows:

$$\epsilon(\rho) \rightarrow 1 \quad \text{as } \rho \rightarrow 0,$$

and

$$\epsilon(\rho) \rightarrow \tilde{C}, \quad \tilde{C} = \frac{1}{\sqrt{\frac{l^2}{\ell^2}(\kappa + \mathcal{E}^2) - 1}} + \sqrt{\frac{\frac{l^2}{\ell^2}(\kappa + \mathcal{E}^2)}{\frac{l^2}{\ell^2}(\kappa + \mathcal{E}^2) - 1}},$$

as $\rho \rightarrow \infty$. Consequently, the behavior of $\phi(\rho)$ is:

$$\phi(\rho) \rightarrow \tilde{\phi}(\rho_i) \quad \text{as } \rho \rightarrow 0,$$

and

$$\phi(\rho) \rightarrow \tilde{\phi}(\rho_i) \pm \frac{\ln(\tilde{C})}{a} \quad \text{as } \rho \rightarrow \infty.$$

These behaviors can be observed in Figure 3, particularly when the initial conditions is neglected, $\tilde{\phi}(\rho_i) = 0$. For rays in this optical background, we derive the corresponding effective potential:

$$V_{\text{eff}}(\rho) = \frac{\ell^2}{l^2 \cosh^2\left(\frac{a}{\ell}\rho\right)}, \quad (5.2)$$

which resembles the classic Pöschl-Teller potential, known for its exact solvability in quantum mechanics. This potential reaches a maximum at $\rho = 0$ and decays rapidly to zero at large radial distances, with the decay rate governed by the radius of the wormhole and constant parameters given by ℓ . These parameters determine the peak strength and control the decay rate. The profile of this effective potential is presented in Figure 2. It represents a purely repulsive interaction, excluding bound-state solutions, and is thus suitable for modeling scattering phenomena, tunneling, and resonance effects.

Next, we analyze wave dynamics in this curved background by solving the corresponding Helmholtz equation. We rewrite the wave equation in a one-dimensional Schrödinger-like form with the purely repulsive effective potential:

$$V_{\text{eff}}(\rho) = \frac{a^2}{4l^2} + \frac{\frac{a^2}{4} + m^2}{l^2 \cosh^2\left(\frac{a}{\ell}\rho\right)}. \quad (5.3)$$

Here, $\frac{l}{a}$ represents the curvature radius of the optical wormhole. The potential exhibits different behaviors at short and large distances, reflecting the geometric properties of the underlying spacetime. As $\rho \rightarrow 0$, the hyperbolic cosine term approaches $\cosh\left(\frac{a}{l}\rho\right) \approx 1$, leading to:

$$V_{\text{eff}}(0) = \frac{a^2}{4l^2} + \frac{a^2/4 + m^2}{l^2}.$$

In this regime, the effective potential tends to a constant value. At large ρ , where $\rho \rightarrow \infty$, the hyperbolic cosine grows exponentially, i.e., $\cosh\left(\frac{a}{l}\rho\right) \approx \frac{1}{2}e^{\frac{a}{l}\rho}$, causing the second term of the potential to decay exponentially. Thus, the effective potential approaches:

$$V_{\text{eff}}(\rho) \rightarrow \frac{a^2}{4l^2}.$$

For large distances, the effective potential tends to a constant value, indicating weakening of the interaction. This suggests that the potential has a short-range component dominated by the second term, while at large distances the first term represents a constant background potential. The characteristic scale of this potential is controlled by the curvature radius $\frac{l}{a}$, which determines the spatial extent over which the potential decays and the overall structure of the optical wormhole.

At the optical origin ($\rho = 0$), the height of the effective potential is predominantly influenced by the magnetic quantum number m , particularly for large m , under a fixed curvature radius. However, this influence diminishes at larger optical distances, despite the background potential remaining non-zero. For large m , the effective potential height can reach substantial values but remains constant with respect to radial distance (see Figure 5). Assuming the wormhole has a radius l at the midpoint ($\rho = 0$), the system can be approximated as a barrier potential with a constant height V_0 and width $L = 2l$ for waves approaching the potential barrier near the optical origin. Within this framework, we analyze the system to determine the reflection (R) and transmission (T) coefficients, which satisfy the condition $T + R = 1$. These coefficients are provided in Eqs. (4.18) and (4.19). The results indicate that the transmission coefficient decreases exponentially with increasing $L = 2l$, corresponding to a larger optical wormhole radius l . Furthermore, the reflection coefficient decreases significantly as L increases. The dependence of these coefficients on the optical wormhole radius is illustrated in Figure 6. Additionally, Eq. (4.18) reveals that the transmission coefficient approaches zero as $k_1 \rightarrow 0$.

Graphene-like structures are widely recognized for their remarkable versatility, allowing them to be curved, rolled, or twisted to meet specific design requirements. This adaptability facilitates precise control over the effective curvature of graphene sheets [12] or graphene-based wormholes [26]. Our findings reveal that the curvature radius of the optical wormhole dictates both the width and magnitude of the effective background potential. This potential may be systematically adjusted and consequently these structures may offer significant potential for applications in advanced photonic and materials-based technologies.

CRedit authorship contribution statement

Semra Gurtas Dogan: Conceptualization, Methodology, Investigation, Writing – Review and Editing, Formal Analysis, Validation, Visualization, Project Administration.

Abdullah Guvendi: Conceptualization, Methodology, Investigation, Writing – Review and Editing, Formal Analysis, Validation, Visualization.

Omar Mustafa: Conceptualization, Methodology, Investigation, Writing – Review and Editing, Formal Analysis, Validation, Visualization.

Data availability

The authors confirm that the data supporting the findings of this study are available within the article.

Conflicts of interest statement

The authors have disclosed no conflicts of interest.

Funding

This research has not received any funding.

References

- [1] M. Banados, C. Teitelboim, J. Zanelli, "Black hole in three-dimensional spacetime" *Physical Review Letters*, **69** 1849 (1992)
- [2] S. Carlip, "The (2+ 1)-dimensional black hole" *Classical and Quantum Gravity*, **12** 2853 (1995)
- [3] F. Ahmed, A. Guvendi, "BTZ black hole in R+ α A gravity and thermodynamic properties" *Chinese Journal of Physics*, **89** 69–85 (2024)
- [4] Y. Liu, Q. Pan, B. Wang, "Holographic superconductor developed in BTZ black hole background with backreactions" *Physics Letters B*, **702** 94–99 (2011)
- [5] A. Guvendi, O. Mustafa, "Investigating quantum criticality through charged scalar fields near the BTZ black hole horizon" *Annals of Physics*, 169897 (2024)
- [6] A. Iorio, G. Lambiase, "The Hawking–Unruh phenomenon on graphene" *Physics Letters B*, **716** 334–337 (2012).
- [7] M. Cvetič, G.W. Gibbons, "Graphene and the Zermelo optical metric of the BTZ black hole" *Annals of Physics*, **327** 2617–2626 (2012).
- [8] B.S. Kandemir, "Hairy BTZ black hole and its analogue model in graphene" *Annals of Physics*, **413** 168064 (2020)
- [9] A. Guvendi, H. Hassanabadi, "Fermion-antifermion pair in magnetized optical wormhole background" *Physics Letters B*, **843** 138045 (2023).
- [10] S.G. Dogan, A. Guvendi, "Weyl fermions in a 2+ 1 dimensional optical background of constant negative curvature" *European Physical Journal Plus*, **138** 452 (2023).
- [11] A. Guvendi, S.G. Dogan, "Vector bosons in the rotating frame of negative curvature wormholes" *General Relativity and Gravitation*, **56** 32 (2024).
- [12] A. Guvendi, S.G. Dogan, O. Mustafa, K. Hasanirrok, "Photonic modes in twisted graphene nanoribbons" *Physica E: Low-dimensional Systems and Nanostructures*, **166** 116146 (2025).
- [13] T. Müller, "Exact geometric optics in a Morris-Thorne wormhole spacetime" *Physical Review D*, **77** 044043 (2008).
- [14] F. dos S. Azevedo, J.D.M. de Lima, A. de Pádua Santos, F. Moraes, "Optical wormhole from hollow disclinations" *Physical Review A*, **103** 023516 (2021).
- [15] Y. Nambu, S. Noda, and Y. Sakai, "Wave optics in spacetimes with compact gravitating object" *Physical Review D*, **100** 064037 (2019).
- [16] S.E. Gralla, A. Lupsasca, "Lensing by Kerr black holes" *Physical Review D*, **101** 044031 (2020).
- [17] J.A.H. Futterman, F.A. Handler, R.A. Matzner, "Scattering from Black Holes" (Cambridge University, (2009) 204 pages).
- [18] M.D. Johnson, A. Lupsasca, A. Strominger, G.N. Wong, S. Hadar, D. Kapec, R. Narayan, A. Chael, C.F. Gammie, P. Galison, D.C.M. Palumbo, S.S. Doeleman, L. Blackburn, M. Wielgus, D.W. Pesce, J.R. Farah, J.M. Moran, "Universal interferometric signatures of a black hole's photon ring" *Science Advances*, **6** eaaz1310 (2020).
- [19] The Event Horizon Telescope Collaboration, "First M87 event horizon telescope results. I. The shadow of the supermassive black hole" *The Astrophysical Journal Letters*, **875** L1 (2019).
- [20] C. Xu, L-G. Wang, "Theory of light propagation in arbitrary two-dimensional curved space" *Photonics Research*, **9** 2486–2493 (2021).
- [21] D. Faccio, F. Belgiorno, S. Cacciatori, V. Gorini, S. Liberati, and U. Moschella, "Analogue Gravity Phenomenology: Analogue Spacetimes and Horizons, from Theory to Experiment" (Springer International Publishing (2013) 460 pages).

- [22] J.R. Muñoz de Nova, K. Golubkov, V.I. Kolobov, J. Steinhauer, "Observation of thermal Hawking radiation and its temperature in an analogue black hole" *Nature*, **569** 688–691 (2019).
- [23] W. Xiao, S. Tao, H. Chen, "Mimicking the gravitational effect with gradient index lenses in geometrical optics" *Photonics Research*, **9** 1197–1203 (2021).
- [24] C. Sheng, H. Liu, S.N. Zhu, D.A. Genov, "Trapping light by mimicking gravitational lensing" *Nature Photonics*, **7** 902–906 (2013).
- [25] A. Guvendi, S.G. Dogan, R.L.L. Vitoria, "Rotational influence on fermions within negative curvature wormholes" *European Physical Journal Plus*, **139** 721 (2024).
- [26] T. Rojjanason, P. Burikham, K. Pimsamarn, "Charged fermion in (2+1)-dimensional wormhole with axial magnetic field" *European Physical Journal C*, **79** 660 (2019).
- [27] S. Batz, U. Peschel, "Linear and nonlinear optics in curved space" *Physical Review A*, **78** 043821 (2008).
- [28] R. Bekenstein, J. Nemirovsky, I. Kaminer, M. Segev, "Shape-preserving accelerating electromagnetic wave packets in curved space" *Physical Review X*, **4** 011038 (2014).
- [29] D. Wang, C. Liu, H. Liu, J. Han, S. Zhang, "Wave dynamics on toroidal surface" *Optica*, **6** 17820–17829 (2018).
- [30] A. Libster-Hershko, R. Shiloh, and A. Arie, "Surface plasmon polaritons on curved surfaces" *Optics Express*, **26** 115–118 (2019).
- [31] G. Della Valle, M. Savoini, M. Ornigotti, P. Laporta, V. Foglietti, M. Finazzi, L. Duo, S. Longhi, "Experimental observation of a photon bouncing ball" *Physical Review Letters*, **102** 180402 (2009).
- [32] O. Mustafa, A. Guvendi, "Klein–Gordon particles in cosmic string spacetime: the noninertial effects of a two-way rotating frame and the associated degeneracies" *European Physical Journal Plus*, **139** 950 (2024).
- [33] A. Cortijo, M.A.H. Vozmediano, "A cosmological model for corrugated graphene sheets" *European Physical Journal Special Topics*, **148** 83–89 (2007).
- [34] G.W. Gibbons, C.M. Warnick, "Universal properties of the near-horizon optical geometry" *Physical Review D*, **79** 064031 (2009).
- [35] A. Guvendi, F. Ahmed, S.G. Dogan, "Relativistic fermions and vector bosons in magnetized three-dimensional space-time with a cosmological constant" *Nuclear Physics B*, **1004** 116569 (2024).